

A New Loss and Deviation Model for Axial Compressor Inlet Guide Vanes

Milan Banjac

e-mail: mbbanjac@mas.bg.ac.rs

Milan V. Petrovic

e-mail: mpetrovic@mas.bg.ac.rs

Faculty of Mechanical Engineering,
University of Belgrade,
Belgrade, Serbia

Alexander Wiedermann

MAN Diesel & Turbo SE,
Oberhausen, Germany

e-mail: alexander.wiedermann@man.eu

This paper describes a new universal algebraic model for the estimation of flow deflection and losses in axial compressor inlet guide vane devices. The model deals with nominal flow and far-off-design operating conditions in connection with large stagger angle adjustments. The first part of the model considers deflection and losses in 2D cascades, taking into account the main cascade geometry parameters and operating conditions, such as Mach number and stagger adjustment. The second part of the model deals with additional deviation and losses due to secondary flow caused by the end wall viscous effects and by the trailing vortices. The model is developed for NACA65 airfoils, NACA63-A4K6 airfoils, and airfoils having an NACA65 thickness distribution on a circular-arc camber line. It is suitable for application in 1D or 2D through-flow calculations for design and analysis cases. The development of the method is based on systematic computational fluid dynamics (CFD) flow calculations for various cascade geometries and operating parameters. The comparison of correlation results with experimental data for several test cases shows good agreement. [DOI: 10.1115/1.4025956]

Introduction

In a compressor, the inlet guide vane (IGV) is unique since it is the only flow accelerating blade row. Due to cascade configurations with lower blade solidities and camber angles, the common loss and deviation correlations for turbine cascades cannot be applied to IGV rows. This is especially valid for exit angle correlations based on the ratio between blade row throat width and blade-to-blade spacing. The sine rule equation is hardly applicable for cascade configurations having lower solidity values.

Also, the secondary flow caused by end wall boundary layers and trailing edge vortices has a large impact on the final exit flow angle in IGV blade rows. Secondary flows induced by the trailing vorticities can have a substantial impact on flows in blade rows having a small number of blades and a low hub/tip radius ratio.

The total pressure losses in IGV rows are generally small. Even IGV rows with a large loss coefficient usually have a small total pressure drop because of small outflow kinetic energy, except in cases with extreme stagger angle adjustments. Therefore, the loss coefficient of IGV is not the most important factor for the prediction of overall machine performance. In contrast, the IGV exit flow angle is of crucial importance for operation of the following stages. It determines amount of the work transferred in the first rotor. The work and the pressure ratio of the first stage determine the axial velocity and the pressure rate for the following stages and for the whole machine.

There are only a few published data on IGV performances. Lieblein studied the performances of thin-sheet inlet guide vanes [1]. Zimmey and Lappi [2] presented data on two-dimensional tests of airfoils in cascades that were mostly used for the design of the compressor entrance vanes. Based on these data, Waltke [3] developed correlations for losses and deviations in IGVs. Petrovic et al. [4] applied these correlations with significant calibration corrections with respect to a through-flow method for axial compressors. However, the results suggested that a new model should be developed.

This paper describes the development of a loss and deflection model for cascades having NACA65 airfoils or airfoils with NACA65 thickness distribution and a circular-arc camber line and NACA63-A4K6 airfoils. Due to the crucial influence on the overall aerodynamic process of the compressor, the deflection correlations are of major importance for accurate mean-line, quasi 2D, or through-flow calculations, for both design and analysis cases.

General Approach

The overall model is divided into several separate correlations:

- basic loss and deviation correlations for 2D cascades with blades having nominal maximum relative thickness and for reference incidence angle flow
- thickness corrections for basic 2D correlations
- additional loss and deviation expressions for stagger angle adjustment with respect to the reference incidence angle, the additional deviation due to secondary flow induced by the trailing edge vortices
- the additional deviations and losses from secondary flows caused by the end wall boundary layers

A two-dimensional cascade is shown in Fig. 1, where the definitions of the camber angle ϕ , the stagger angle γ , and the metal angles κ_1 and κ_2 are presented. Two other important cascade parameters are the blade solidity $\sigma = c/s$ and the blade relative thickness t/c .

Correlations for Reference Incidence

In contrast to turbine cascade correlations, here the inlet Mach number Ma_1 is used instead of the exit value. Also, the total pressure loss coefficient is defined over the inlet dynamic pressure $\varpi = \Delta p^\circ / (p_1^\circ - p_1)$. Every set of parameters ϕ and σ determines the reference incidence angle $i_0 = f(\phi, \sigma)$ with corresponding reference deviation $\delta_0 = f(\phi, \sigma, Ma_1)$ and reference total pressure loss coefficient $\varpi_0 = f(\phi, \sigma, Ma_1)$. In all considerations in this paper, the purely axial inflow is assumed: $\alpha_1 = 0$ deg.

NACA65 Airfoils. For airfoils with NACA65 camber line and circular-arc camber line, we have the following relations between

Contributed by the International Gas Turbine Institute (IGTI) of ASME for publication in the JOURNAL OF TURBOMACHINERY. Manuscript received September 13, 2013; final manuscript received October 15, 2013; published online January 2, 2014. Editor: Ronald Bunker.

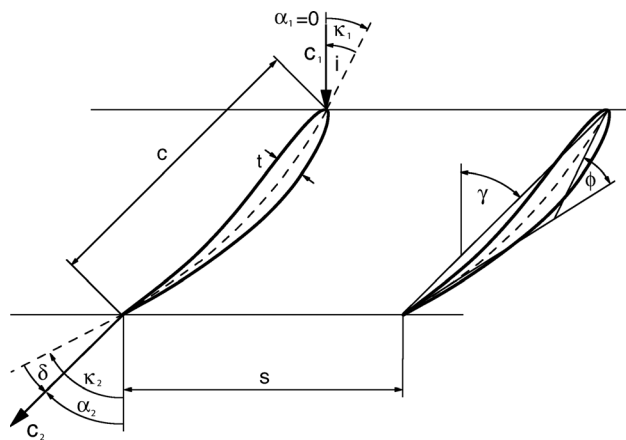


Fig. 1 Two-dimensional IGV cascade geometry

Table 1 Parameters varied for NACA65 cascades (original and circular-arc camber line)

ϕ (deg)	σ (deg)	t/c	Ma_1
0, 10, 20, 30, 40	0.6, 0.8, ..., 1.8	0.1	0.2, 0.4, 0.5
Re_c	Tu (%)	α_1 (deg)	$AVDR$
$5 \cdot 10^5$	2	0	1

the camber angle ϕ , the stagger angle γ , and the metal angles κ_1 and κ_2 :

$$\kappa_1 = \gamma - \phi/2 \quad \kappa_2 = \gamma + \phi/2 \quad (1)$$

The metal angles for NACA65 camber lines are defined using the equivalent circular-arc camber line as in Ref. [5]. Lieblein's correlation for reference incidence [5] was selected as a basis for the new overall model. For defined cascade solidity σ , blade camber angle ϕ , and inlet flow angle $\alpha_1 = 0$ deg, the reference incidence angle is

$$i_0 = (0.025 \cdot \sigma - 0.06) \cdot \phi \quad (\text{deg}) \quad (2)$$

Equation (2) is in good agreement with reference incidence data for an IGV cascades by Zimney and Lappi [2].

The reference metal angles for $\alpha_1 = 0$ deg are

$$\kappa_{1,0} = i_0 \quad \kappa_{2,0} = \phi + i_0, \quad (3)$$

In order to develop loss and deviation functions, a series of calculations of cascade flows were carried out using the MISES viscous solver [6]. Similar approaches were used for compressor cascades in Refs. [7] and [8]. Ranges of parameters that were varied are given in Table 1. An example of the calculation grid is shown in Fig. 2.

The turbulence level was chosen according to Ref. [9], although it does not have a significant impact on deviation.

Figure 3 shows MISES results for the NACA65 cascades and Fig. 4 shows analogous results for cascades having a NACA65 thickness on circular-arc camber lines. The curve fit of the MISES data gave the correlation

$$\delta_0 = (a + b \cdot \sigma + c \cdot Ma_1) \cdot \phi^{(d+e \cdot \sigma + f \cdot Ma_1)} \quad (4)$$

The equation is not defined for negative values of ϕ , so the input value should be limited to $\phi := \max(0, \phi)$. The same equation is

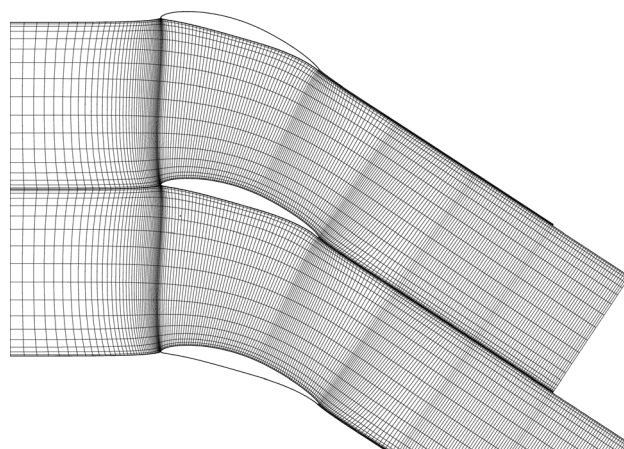


Fig. 2 MISES calculation grid for NACA65 cascade

used for both NACA65 cascades with original camber lines and NACA65 cascades with circular-arc camber lines. The coefficients in Eq. (4) are given in Table 2.

The equation for reference loss is

$$\omega_0 = \exp(a + b \cdot \phi + c \cdot \sigma + d \cdot Ma_1) + e \cdot \sigma \quad (5)$$

with coefficients given in Table 3.

Additional calculations with variation of blade thickness were carried out in order to develop corrections for the thickness. Thickness and solidity were varied for constant camber angle cascades with $\phi = 40$ deg. As Fig. 5 shows, the change of the deviation is approximately a linear function of thickness and solidity. This is valid for incompressible flow, $Ma = 0.2$, and also for flow with higher Mach number value, $Ma = 0.4$.

Based on these results and assuming that the correction is proportional to the camber angle value, simple expressions were established:

$$\Delta \delta_t = (3 + 9.44\sigma)(0.1 - t/c) \frac{\phi}{40} (2Ma_1 + 0.6) \quad (6a)$$

$$\Delta \omega_t = (0.0429 - 0.0704\sigma)(0.1 - t/c)(6.7Ma_1 - 0.34) \quad (6b)$$

where the Mach number value is limited to $Ma_1 := \max(Ma_1, 0.2)$.

NACA63—A4K6 Airfoils. The NACA A4K6 airfoils have maximum camber at 0.373 of relative chord length. For an airfoil with lift coefficient $C_{l0} = 1$, the relative maximum camber is 0.058416. The camber is proportional to the lift coefficient value. For this type of airfoil, the sections are usually defined using the lift coefficient and stagger angle. The equivalent parabolic camber line is used to define the metal angles as in Ref. [10]

$$\kappa_1 = \gamma - \arctg(0.4749C_{l0}) \quad \kappa_2 = \gamma + \arctg(0.1549C_{l0}) \quad (7)$$

The camber line angle can be calculated as

$$\phi = \arctg(0.4749C_{l0}) + \arctg(0.1549C_{l0}) \quad (8)$$

A useful tool is the approximated inverse function of Eq. (8)

$$C_{l0} = -3.6529 \ln(1 - 0.006975\phi) \quad (9)$$

where angle ϕ is in degrees. For the A4K6 airfoil MISES calculations, the single airfoil lift coefficient C_{l0} was selected as the basic input parameter, and it was varied as shown in Table 4. The basic relative thickness was set to be 0.06, as in Ref. [11], and a series

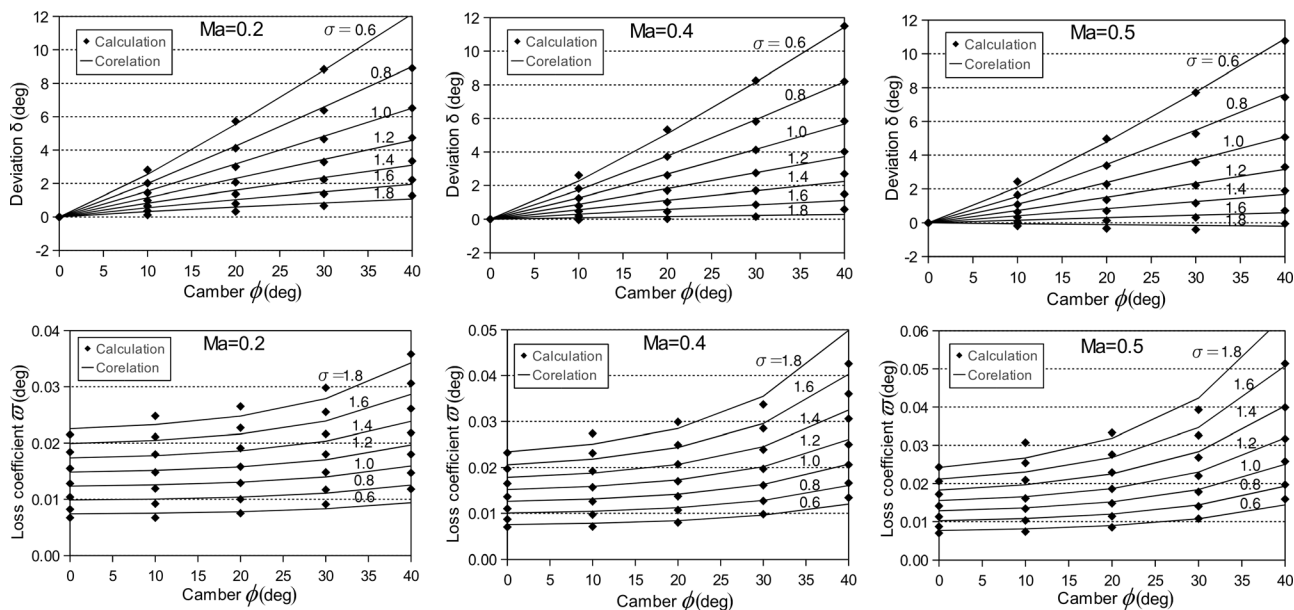


Fig. 3 Results of MISES calculations for the reference incidence—NACA65 airfoil cascade

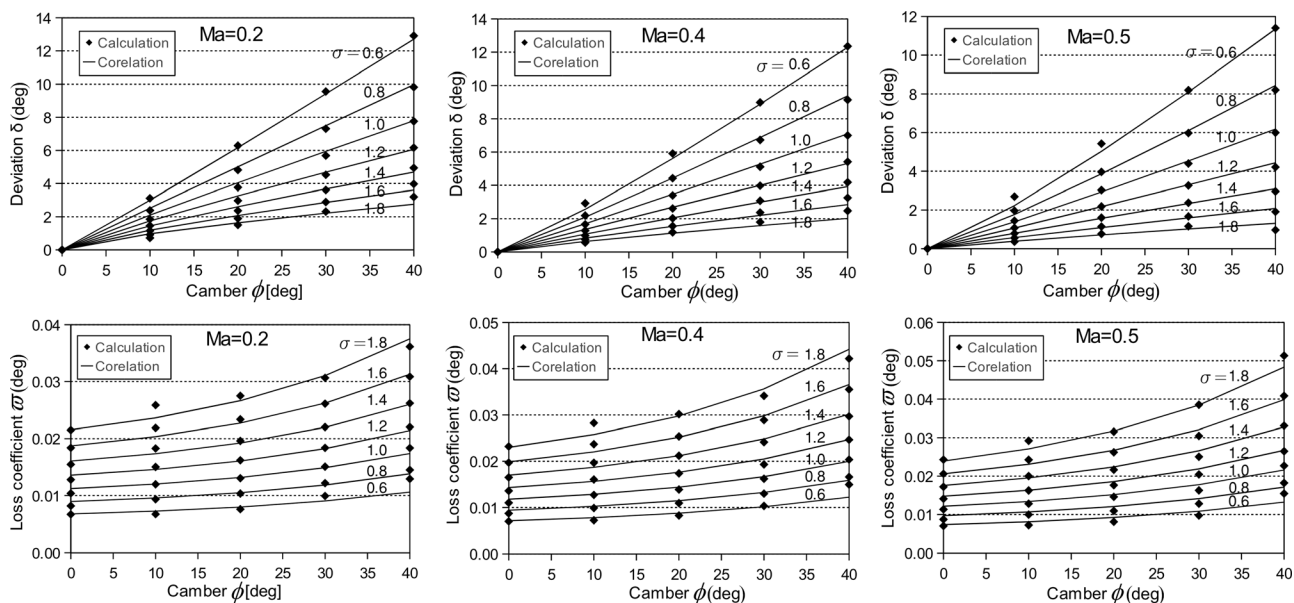


Fig. 4 Results of MISES calculations for the reference incidence—circular camber line airfoils with NACA65 thickness

Table 2 Coefficients for the reference deviation according to Eq. (4)

	NACA65	NACA65 Circ.	A4K6
<i>a</i>	0.293615	0.401695	0.1002060
<i>b</i>	−0.119002	−0.081487	−0.0443672
<i>c</i>	−0.172188	−0.408090	−0.0675766
<i>d</i>	1.226289	1.101494	1.3524830
<i>e</i>	−0.224200	−0.244558	−0.2510492
<i>f</i>	0.192262	0.440575	0.1684732

Table 3 Coefficients for the reference loss, Eq. (5)

	NACA65	NACA65 Circ.	A4K6
<i>a</i>	−10.75333	−7.83636	−12.57281
<i>b</i>	0.0720483	0.0380755	0.0789899
<i>c</i>	1.481823	1.186934	1.917747
<i>d</i>	4.076325	1.41946	3.68047
<i>e</i>	0.0121276	0.00951139	0.0139719

of MISES calculations were performed using same flow parameters as in the NACA65 case. An example MISES grid is shown in Fig. 6.

The reference stagger angle is

$$\gamma_0[\text{deg}] = 17.702C_{l0}/(1 + 0.4987\sigma^{-1.0724}) \quad (10)$$

Equation (10) is based on the graphical data from Ref. [11] for minimum loss stagger for A4K6 cascades, and for $\alpha_1 = 0$ deg. The reference incidence is then

$$i_0 = \kappa_{1,0} = \gamma_0 - \text{tg}(0.4749C_{l0}) \quad (11)$$

For the reference loss and deviation, the same functions as in the NACA65 case were used. The reference deviation

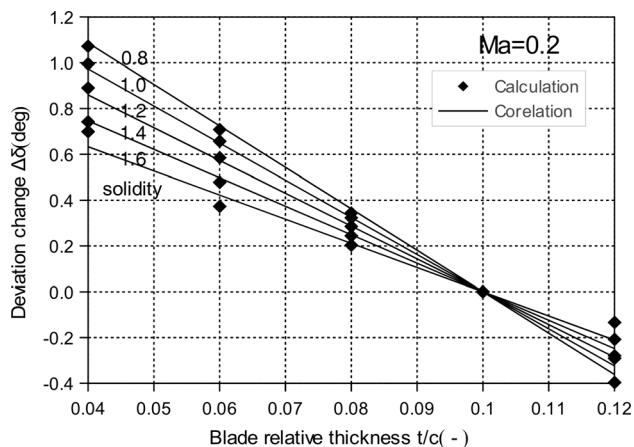


Fig. 5 Deviation correction for blade thickness, NACA65 airfoil cascade with 40 deg camber angle

Table 4 Parameters for the reference deviation and the reference loss coefficient

C_{l0}	σ (deg)	t/c	Ma_1 (deg)
0.0, 0.6, ..., 2.4	0.6, 0.8, ..., 1.8	0.06	0.2, 0.4, 0.5

$\delta_0 = f(\phi, \sigma, Ma)$ is given by Eq. (4) and the reference loss coefficient $\varpi_0 = f(\phi, \sigma, Ma)$ by Eq. (5). Appropriate values of the coefficients for these equations are given in Tables 2 and 3. The input camber angle is calculated using Eq. (7).

Both equations are presented graphically in Fig. 7.

The thickness correction is developed on the basis of calculations for airfoils with a constant camber of $\phi = 56$ deg ($C_{l0} = 1.8$)

$$\Delta\delta_t = (4.7 + 12.55\sigma)(0.06 - t/c) \frac{\phi}{56} (2.2Ma_1 + 0.56) \quad (12a)$$

$$\Delta\varpi_t = (0.0621 - 0.1006\sigma)(0.06 - t/c) \cdot 5Ma_1 \quad (12b)$$

As mentioned earlier, the basic thickness for A4K6 correlations is $t/c = 0.06$.

Correlations for Nonreference Stagger Angle

For NACA65 cascades, if the geometry is specified using metal angles, for $\sigma = c/s$ and $\phi = \kappa_2 - \kappa_1$ the reference incidence $i_0 = i_0(\phi, \sigma)$ can be calculated using Eq. (2). Corresponding to incidence i_0 we have the reference stagger angle γ_0 , while the actual stagger γ can be different

$$\gamma_0 = \phi/2 + i_0 \quad \gamma = (\kappa_1 + \kappa_2)/2 \quad (13)$$

For A4K6 cascades, the stagger angle is usually defined, and the actual stagger can be found using Eq. (10).

The term *adjustment* is used for both types of profiles to designate the difference between the actual and the reference incidence angle

$$\Omega = \gamma - \gamma_0 = i - i_0 \quad (14)$$

The term refers to any declination of the incidence angle from its reference value. Adjustment may be the result of a design and a nonreference blade staggering and/or of additional blade angle turning due to demands of the compressor regulation.

For the stagger angle adjustment Ω , there are additional deviations and additional losses

$$\delta_{2D} = \delta_0 + \Delta\delta_t + \Delta\delta_\Omega \quad \varpi_{2D} = \varpi_0 + \Delta\varpi_t + \Delta\varpi_\Omega \quad (15)$$

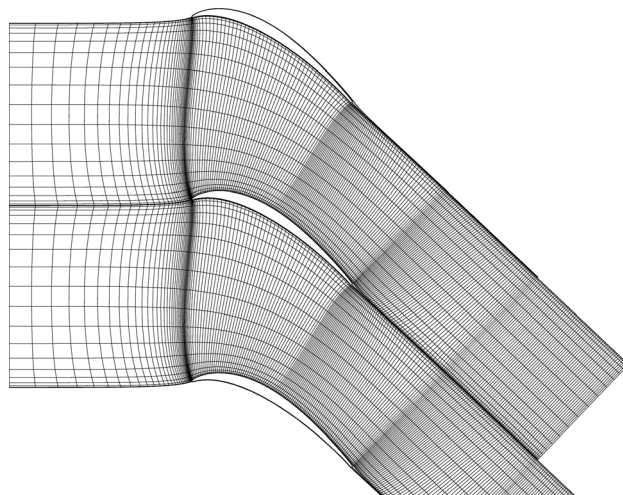


Fig. 6 MISES calculation grid for NACA63 A4K6 cascade

The equation for additional deviation due to stagger adjustment is

$$\Delta\delta_\Omega = (a + b\phi^2 + c\sigma + d\sigma^2 + e\phi \cdot \Omega^f) \cdot \Omega \quad (16)$$

with coefficients given in Table 5.

Equation (16) can be used for all airfoil types mentioned in this paper. It is based on the data from the MISES calculations for NACA65 cascades. Calculations were performed for the parameters varied in the range shown in Table 6. Figure 8 shows the deviation angle changes due to adjustment with examples for two different camber angles.

Cascades with solidity $\sigma = 0.6$ were not taken into account in order to achieve a better fit of data in the solidity range that is more important for practice ($\sigma = 0.8 - 1.8$). The axial velocity density ratio is $AVDR = 1$ in all cases.

Because of convergence problems with some configurations, all the calculations for adjusted rows were done for inviscid flows (including unadjusted cases). The results were used to obtain the $\Delta\delta_\Omega$ function (16).

A correlation for additional total pressure loss due to stagger angle adjustment was created based on a series of 3D CFD calculations and on the authors' experience based on through-flow calculations

$$\begin{aligned} \Delta\varpi_\Omega &= 0.0002 \cdot 1.48^\Omega \cdot 0.09^\sigma \cdot (1 + 0.01 \cdot \phi) \\ \Delta\varpi_{\text{stall}} &= 0.12 + 0.007\phi \end{aligned} \quad (17)$$

The value for the off-design loss should be limited

$$\Delta\varpi_\Omega := \min(\Delta\varpi_\Omega, 1.2\Delta\varpi_{\text{stall}}) \quad (18)$$

to avoid numerical problems in calculations. The limiting value is arbitrary but it should not exceed the stall value excessively.

Comparison of 2D Correlations With 3D Flow Results

In this section, 2D correlations for deviation are compared with 3D CFD results. For this comparison, the IGV of the experimental three-stage highly loaded compressor at the Leibniz University of Hanover (LUH) described in Ref. [12] was selected. The IGV device has 26 blades with NACA65 profiles and hub/tip radius ratio $R_H/R_T = 0.429$. The blades are highly twisted with the exit metal angle increasing from about 0 deg at the hub to about 50 deg at the shroud. The solidity decreases from 2.26 at the hub to 0.97 at the shroud. The geometry of the IGV blades is shown in Fig. 9.

The inlet Mach number was $Ma_1 = 0.375$ and the Reynolds number (based on the chord length and the inlet velocity) was $Re_c \approx 0.32 \cdot 10^5$.

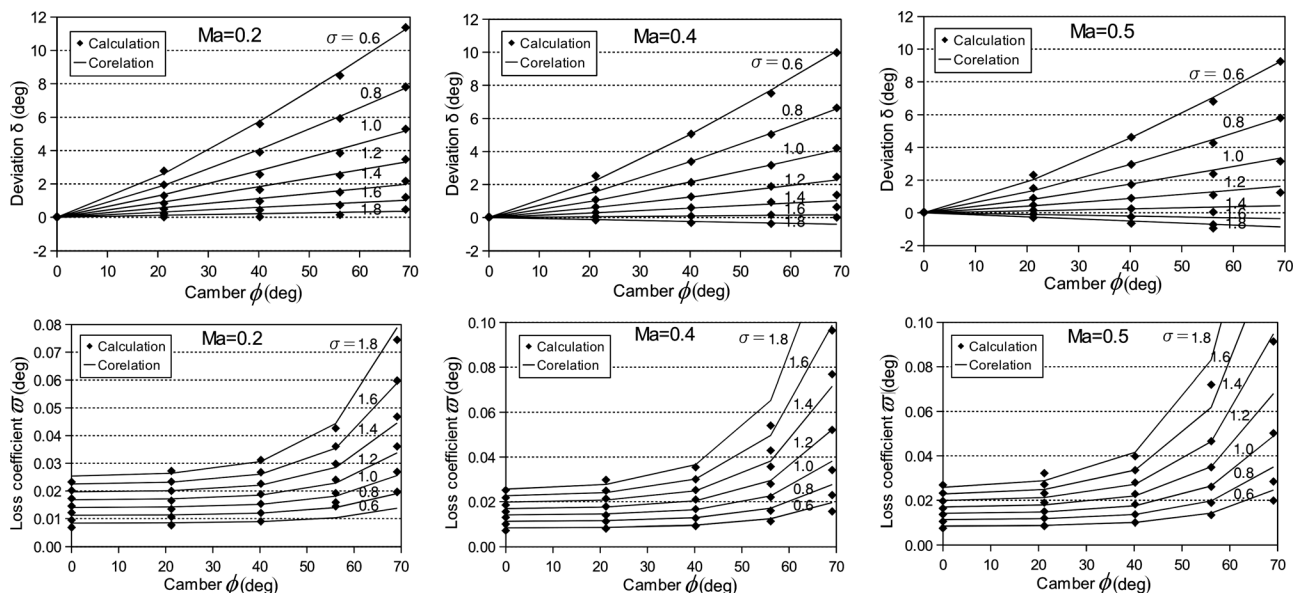


Fig. 7 Results of MISES calculations for the reference incidence—NACA63 A4K6 airfoil cascade

Table 5 Coefficients of Eq. (16) for additional deviation due to stagger adjustment

	$\Omega \leq 0$	$\Omega > 0$
a	0.205450	0.272548
b	2.9165×10^{-5}	3.7159×10^{-5}
c	-0.313651	-0.411102
d	0.090360	0.126291
e	0.0	7.6708×10^{-8}
f	0.0	2.630323

Table 6 Range of variation of parameters for MISES calculations with stagger adjustments

ϕ (deg)	σ (deg)	Ω (deg)	Ma_1
0, 10, 20, 30, 40	0.8, 1.0, ..., 1.8	-10, 0, 10, 20, 40	0.2

A few Reynolds-averaged Navier–Stokes calculations were carried out using the CFX and SST turbulence model on a mesh with about 1.7×10^6 cells and 140 cells in the spanwise position. The mesh size and density were designated to provide $y^+ < 1$ and the cell height expansion rate was > 1.15 (for all wall boundaries).

Variation of the inlet turbulence from 1% to 5% had a negligible influence on deviations and losses. Calculations with free-slip conditions on the end walls (hub and shroud) were carried out first to obtain a flow field without viscous secondary flows. The results were more appropriate for a comparison with the 2D correlation predictions. The real-flow simulation with no-slip conditions at all walls was carried out for 1% and 4% inlet blockage. The exit flow distribution is shown in Fig. 10.

Blockage was modeled using a constant inlet velocity c_{ae} in the midspan area with the power law $c_a = c_{ae}(y/\delta)^{1/7}$ distribution in the boundary layer zones where the layer thickness is $\delta = 8\delta^*$.

Figure 10 shows a comparison of 3D CFD calculation results for an exit flow angle with the developed 2D correlation and the correlation by Walke [3] based on data given by Zimmey and Lappi [2].

There is a large difference between the results of the 3D calculation with free-slip end walls and the developed 2D correlation in the near-shroud zone. Additionally, a series of blade-to-blade CFX calculations were performed for a number of 2D sections for

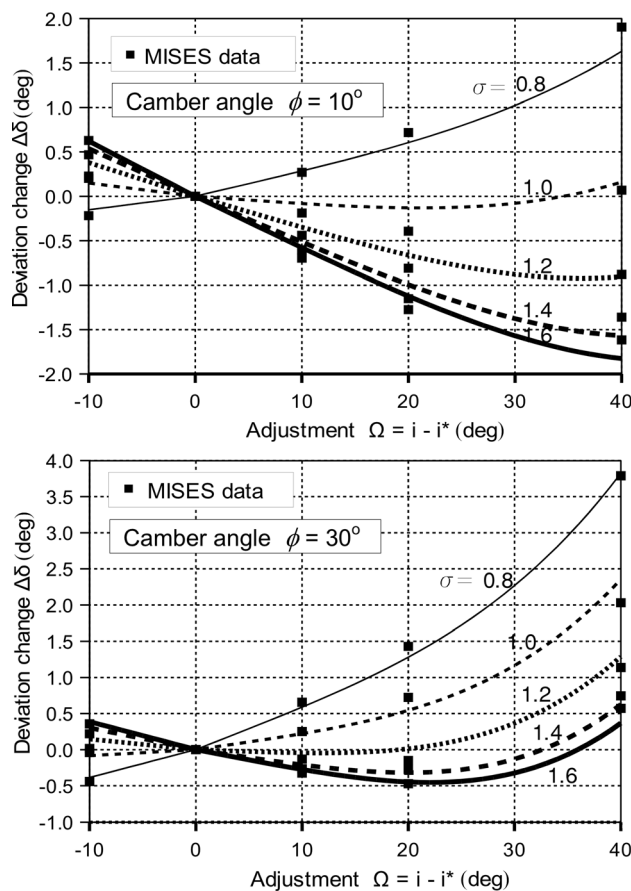


Fig. 8 Additional deviations due to stagger angle adjustment

this cascade. Figure 11 shows the computational grid for 2D CFD calculations. The results are plotted in Fig. 10 and show good agreement with the 2D correlations (Eq. (15)).

The large mismatch between the 2D and 3D results in the near-shroud region could not have been caused only by the AVDR influence, although the AVDR number varies from a value of one in the range $\pm 5\%$. The exit flow angle mismatch is caused by the

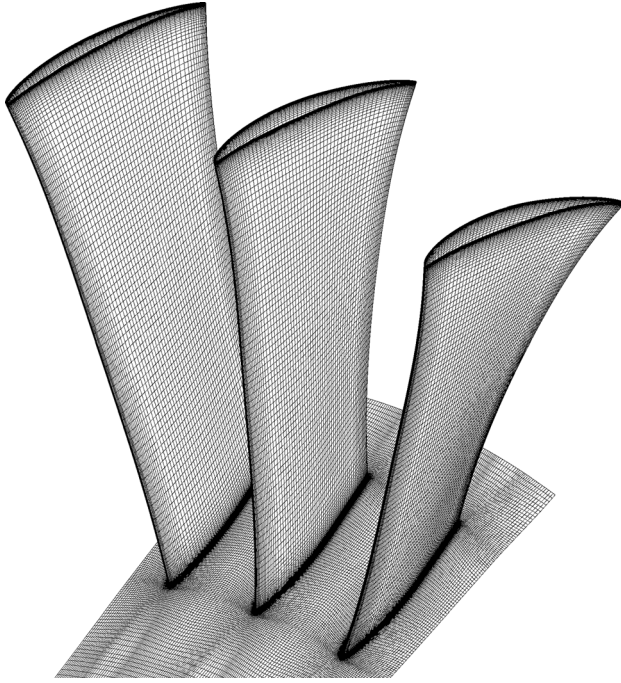


Fig. 9 Grid for twisted IGV blades of the LUH three-stage compressor

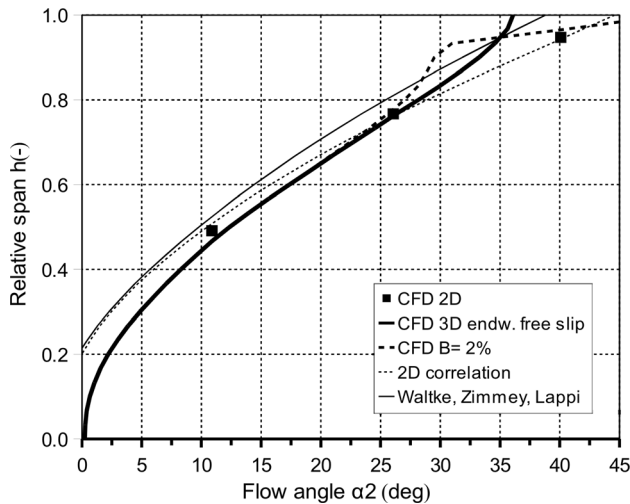


Fig. 10 IGV exit flow angle of the LUH three-stage compressor

existence of intense secondary flows, induced by the exit plane trailing vortices. This process is dominant because of the large blade twist and high spanwise variation of the exit flow direction. An additional model to simulate this influence is necessary to be added to the 2D correlations.

Secondary Deviation Caused by Induced Flows

Basic Considerations. Since an IGV row usually has a small number of blades and a low hub-to-shroud radius ratio, a spanwise change of blade circulation can induce intense secondary flows with a significant impact on the IGV flow exit angles.

If we observe a ring of thickness dR on a vane trailing edge plane (Fig. 12), the velocity circulation on the ring contour is

$$d\Gamma = 2\pi(r - dr)(c_u - dc_u) - 2\pi rc_u \approx 2\pi d(rc_u)$$

Per blade, that is: $2\pi/n \cdot d(rc_u)$. This circulation is actually a spanwise change of blade circulation $d\Gamma = d\Gamma_{\text{blade}}$

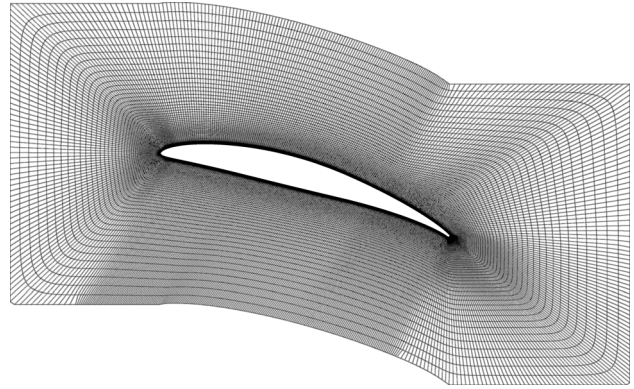


Fig. 11 Grid for CFD 2D cascade flow calculations

$$\Gamma_{\text{blade}} = s(c_{2u} - c_{1u}) = \frac{2\pi r}{n} \cdot c_{2u}$$

The local change of the blade circulation produces the same amount of circulation in the trailing edge (TE) plane TE as shown in Fig. 12. This amount of TE plane circulation is forced around the local TE vortex filament. The velocity induced by a single, semi-infinite, vortex filament of finite circulation Γ is

$$c^{\text{ind}} = \frac{\Gamma}{4\pi} \int_0^{\pi/2} \cos \varphi d\varphi = \frac{\Gamma}{2\pi d}$$

It is valid when the filament direction is perpendicular to the plane that contains the point o and the filament beginning as shown in Fig. 13. The sign convention for the circulation and the induced velocity is chosen such that a positive value of induced velocity corresponds to a positive value of deviation and that the spanwise growth of blade circulation gives a positive circulation in the trailing plane.

A linear cascade is considered here. To calculate the overall value of induced velocity, we can use the system of distributed (continuously or discrete) vortex filaments, each of circulation $\Delta\Gamma_i$ similarly as in Ref. [13]. Along the trailing edge, the induced velocity has only a pitchwise component

$$c_x^{\text{ind}} = \frac{1}{2\pi} \int_0^H \frac{1}{y_o - y_i} d\Gamma \approx \frac{1}{2\pi} \sum_i \frac{1}{y_o - y_i} \Delta\Gamma_i$$

where y is a spanwise coordinate as shown in Fig. 13. Basically, we are interested only in the x component of the induced velocity because the spanwise flow does not affect the exit flow angle value α_2 . In the final model, the distribution of the induced velocity along the trailing edge is calculated numerically and that result is used to find the spanwise distribution of the exit angle deviation.

Hub and shroud flow field mirror images have to be added to the basic model to simulate the end walls. Also, the influence of trailing edges of neighboring blades has to be included. Details of derivation of the final model are given in Appendix A.

Induced Flow Correlation. Final correlation for the induced velocity at local point o is (see Fig. 14)

$$\left. \frac{c_x^{\text{ind}}}{c_a} \right|_o = C \frac{1}{2n} \sum_{i=2}^{N-1} \gamma_i \ln \left| \frac{(r_o - r_l)(r_o - 2r_H + r_l)(r_o - 2r_T + r_l)}{(r_o - r_u)(r_o - 2r_H + r_u)(r_o - 2r_T + r_u)} \right|$$

$$r_l = (r_i + r_{i-1})/2, \quad r_u = (r_{i+1} + r_i)/2 \quad (19)$$

In this equation, vortex panels next to the hub and next to the shroud are not taken into account. The circulation change factor

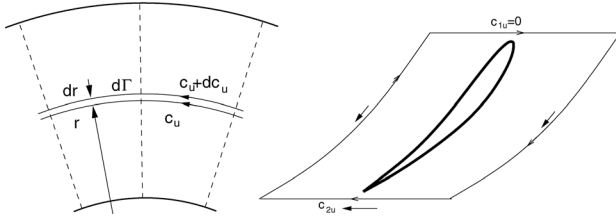


Fig. 12 Exit plane and blade circulation

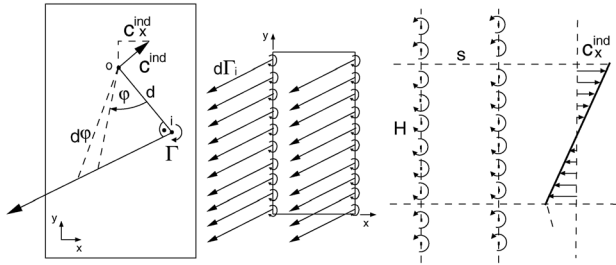


Fig. 13 Single vortex filament ray and the model for a linear cascade

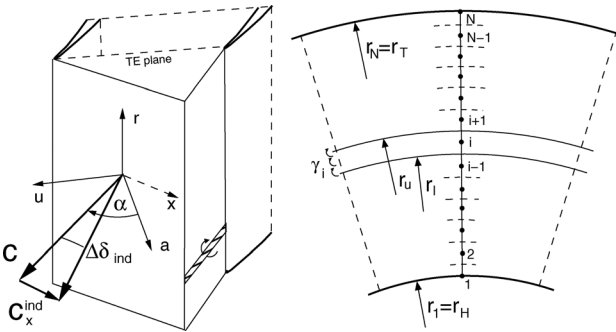


Fig. 14 Exit plane nomenclature (left) and radius nomenclature (right)

(see Appendix A) is expressed using the central finite difference equation

$$\gamma_i = (r_{i+1} \tan \alpha_{2,i+1} - r_{i-1} \tan \alpha_{2,i-1}) / (r_{i+1} - r_{i-1}) \quad (20)$$

where $\alpha_{2,i}$ is the 2D exit flow angle for a spanwise location i calculated using Eq. (16). It is not required that the radial positions i are equidistant, as in Fig. 14.

The correction coefficient (see Appendix A) is

$$C = K \cdot C_{amp} C_{av} = 0.261 \cdot (H/s) (h(1-h))^{0.3308} \quad (21)$$

The value of the factor H/s can be taken at the mean radius or, as done in this work, at a local radius: $H/s = n(r_T - r_H) / (2\pi r_o)$, where n is the number of blades in the row.

Finally, the expression for the local deviation is

$$(\Delta \delta_{ind})_o = \arctg \left(\cos \alpha_{2,o} \cdot \frac{c_x^{ind}}{c_a} \right) \quad (22)$$

where $\alpha_{2,o}$ is the 2D exit flow angle for the local radius, Eq. (16). The values of the deviations for hub ($i=1$) and tip ($i=N$) obtained from Eq. (20) are grid dependent. Therefore, these values should be calculated using extrapolation

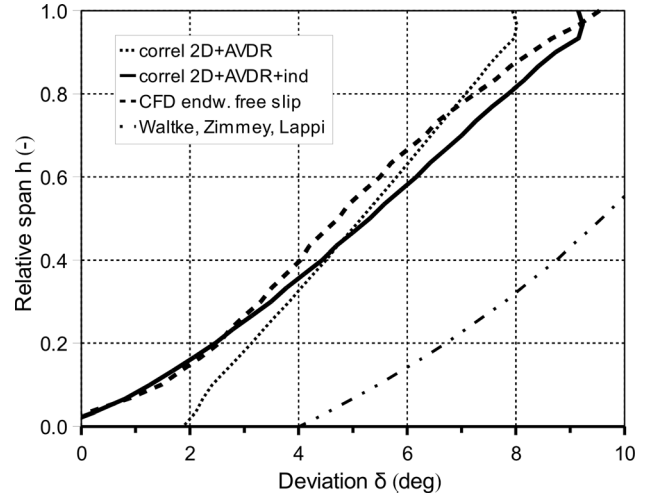


Fig. 15 Induced deviation for a row with an approximately constant exit flow angle over the span for IGVs of the Sulzer four-stage compressor

$$\delta_1 = \delta_2 - \frac{\delta_3 - \delta_2}{r_3 - r_2} (r_2 - r_1), \delta_N = \delta_{N-1} + \frac{\delta_{N-1} - \delta_{N-2}}{r_{N-1} - r_{N-2}} (r_N - r_{N-1}) \quad (23)$$

Here, for example, δ_1 is a shortened form for the deviation $(\Delta \delta_{ind})_1$.

Validation of Induced Flow Model. To compare the induced flow correlation with experimental data, the well-known AVDR correction is introduced

$$\Delta \delta_{AVDR} = 10 \cdot (AVDR - 1) \quad (24)$$

The expression for the deviation, which includes the 2D effects; AVDR influence; and induced flows, can be written as follows:

$$\delta = \delta_0 + \Delta \delta_{\Omega} + \Delta \delta_i + \Delta \delta_{AVDR} + \Delta \delta_{ind}$$

The first test case is the IGVs of the Sulzer four-stage compressor [14]. It has thick blades with $t/c = 1.2$. The solidity varies from 1.54 to 0.73 from hub to tip and the exit metal angle κ_2 changes over a small range from 31 deg to 39 deg. The exit flow angle remains approximately constant over the whole span (about 30.5 deg). Figure 15 shows the induced deviation predicted by the correlation and comparison with the 3D CFD results that are obtained from calculations with free-slip conditions on the end walls. The AVDR number varies from 1.11 at the hub to 1.05 near the shroud.

The next test case is IGVs of the LUH three-stage compressor, which has already been described. The 3D CFD calculation was performed applying free-slip conditions on the end walls. The significant blade twist causes intense induced flows and large discrepancies between the 2D and 3D results. Comparison between the correlation with the induced flow model and the CFX results (Fig. 16) shows good agreement. The AVDR correction has important (but not crucial) merit for the good prediction of deviations in this case. The AVDR number is 1.02 near the shroud, 1.13 at midspan, and as high as 1.18 near the hub.

The difference between the CFD results and prediction by the correlation in the near-shroud region is caused by fact that the model does not take into account vorticities in the region $r \in [r_{N-1}, r_N]$, near the shroud itself. There are several reasons for that. First, to simplify the model, the value of the factor γ_i cannot be calculated by the finite difference central equation at the hub or shroud position. Second, in real flow, the end wall zone trailing vorticity will be suppressed by the end wall boundary layer.

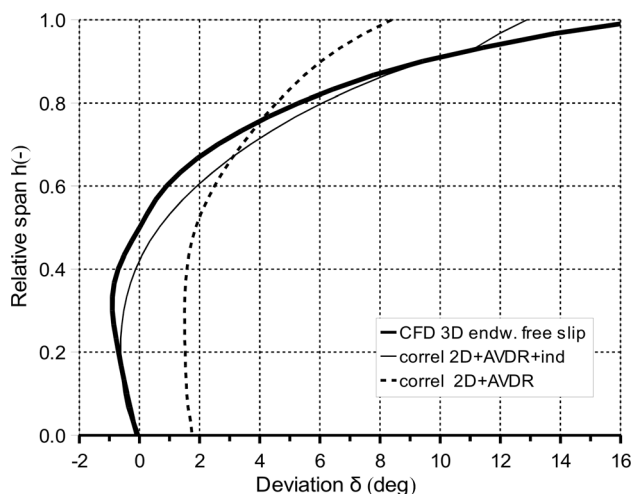


Fig. 16 Induced deviation for a row with highly twisted blades and spanwise increase of blade circulation

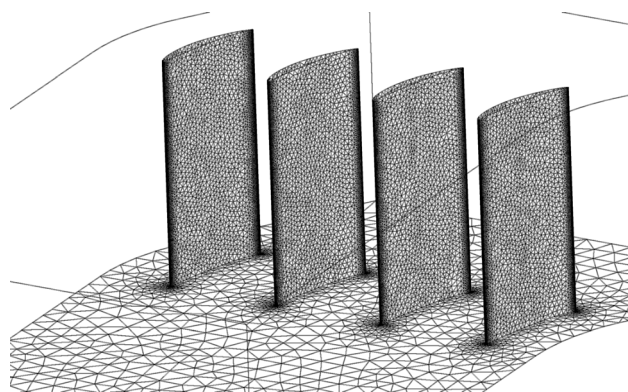


Fig. 17 Model of a linear cascade

Viscous Secondary Flows

The classical approach with algebraic correlations was applied for the viscous secondary flow losses and deviations. These equations can be used individually and independently of the rest of the overall model presented in this paper.

A series of 3D calculations for linear and annular cascades were carried out to study secondary flows induced by the end wall boundary layers. An example of a linear cascade is shown in Fig. 17. The cascade is made of NACA65-10 airfoils whose parameters are given in Table 7.

Incidence angle is according to Eq. (2). The inlet blockage was varied from 2% to 8% ($B = 0.01$ to $B = 0.08$). The cascade model mesh consists of $\sim 1.7 \times 10^6$ of cells per blade, where the mesh density was chosen to give $y^+ < 1$ and a cell expansion rate under 1.2 on all walls. Inlet blockage was simulated, as described earlier, by prescribing the inlet velocity power law distribution in the end wall boundary layer zones. The inlet Mach number was 0.3 and the Reynolds number was $Re_c \approx 5 \cdot 10^5$.

The results are shown in Fig. 18. Among others, these results were used to create the final equation for additional secondary deviation

$$\Delta\delta_{sec} = 1.51C_{\kappa 2}(1 - e^{-0.032\Delta x})[\xi(h) + \xi(1-h)] \quad (25)$$

The correction coefficient $C_{\kappa 2}$ is introduced to include the influence of blade metal angle twist

$$C_{\kappa 2} = 1 + 0.001(h - 0.5) \frac{d\kappa_2}{dr} \quad (26)$$

Table 7 Parameters of the linear cascade model

κ_1 (deg)	κ_1 (deg)	σ	h (mm)	c (mm)
-1.4	38.6	1	140	70

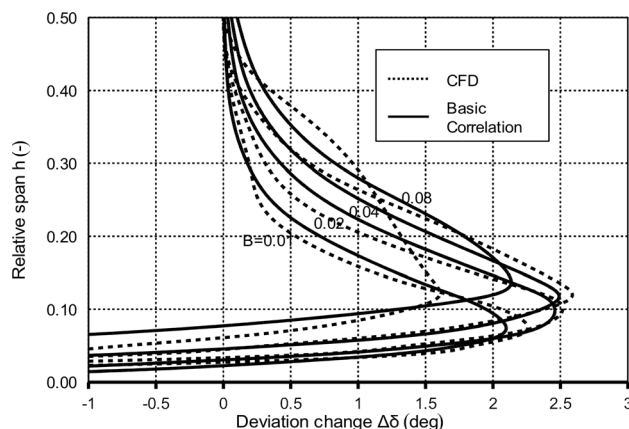


Fig. 18 Basic distribution of the additional deviation

Table 8 Coefficients for Eq. (27)

a	148.912	d	-0.774441
b	890.134	e	-2.3248E-07
c	0.985480	f	2.4796E-05

The metal angle change rate $d\kappa_2/dr$ [deg/m] can be taken to be zero for almost straight or moderately twisted blades. Blade lean can influence secondary deviation to a large extent, as reported elsewhere, e.g., Ref. [15]. However, trailing edge lean in the case of constant profile blades acts on a fluid in a different way to trailing edge lean in the case of twisted blades. An increase in stagger angle from midspan to end wall will amplify secondary deviation. Equation (26) was created using a series of 3D CFD calculations.

The distribution function $\xi(h)$ is

$$\xi(h) = (a + bB)\ln(c + d \cdot B + h^*) \cdot (e + fB)^{h^*} \quad (27)$$

The blockage factor is $B = (\pi\delta_H^* D_H + \pi\delta_T^* D_T)/A_{\text{annulus}}$, and corrected relative spanwise position is $h^* = 0.6(H/s)h$. For practical use of function $\xi(h)$, it is important to limit the value of the blockage to $B := \max(B, 0.01)$. Coefficients for Eq. (27) are given in Table 8.

The basic form of Eq. (27) was derived using CFD results, the effects of which are shown in Fig. 18. Corrected spanwise position h^* was introduced later to include an influence of the cascade aspect ratio and to achieve better agreement with annular row test cases. The near wall overturning from the CFD results is ≈ -14 deg in all cases, while the correlation gives less extreme values (for example: -8.59 deg for $B = 0.04$).

Figure 19 shows a comparison between the correlation and CFD results for an annular cascade with the main parameters $r_H/r_T = 0.59$, $H/c = 2.86$, and $n = 26$ blades. The blade solidity decreases from the hub to the shroud in the range 2.1–0.9. The span height to blade spacing ratio decreases in the range $H/s = 4 - 1.7$ from the hub to the shroud.

The correlation for secondary losses in IGV rows was created using the results from several CFX 3D calculations

$$\Delta\varpi_{sec} = 0.0064 \cdot 1.026^{\Delta x}(s/H) \cdot \eta(h) \quad (28)$$

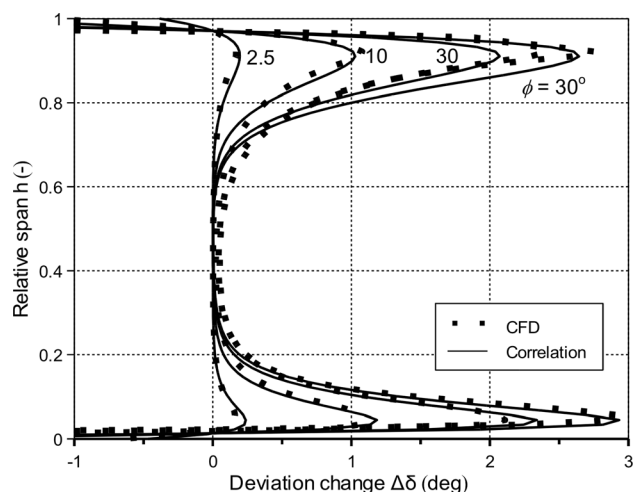


Fig. 19 Correlation for secondary flow deviations applied to a 3D cascade

where $\eta(h)$ is the secondary loss distribution function

$$\eta(h) = 6e^{-8h} - 4e^{-16h} + 6e^{-8(1-h)} - 4e^{-16(1-h)} \quad (29)$$

The spanwise distribution function $\eta(h)$ is selected to have a value of the spanwise integral equal to unity (the actual value is 0.9995). Therefore, this function is suitable for the spanwise distribution of losses calculated using any 1D secondary flow loss model.

Final Loss and Deviation Model and Validation

The final deviation should be calculated using the following expression:

$$\delta = \delta_0 + \Delta\delta_t + \Delta\delta_\Omega + \Delta\delta_{AVDR} + \Delta\delta_{ind} + \Delta\delta_{sec} \quad (30)$$

and the final equation for the total pressure loss coefficient is

$$\varpi = \varpi_0 + \Delta\varpi_t + \Delta\varpi_\Omega + \Delta\varpi_{sec} \quad (31)$$

The validation of the presented model was done by comparison of the results obtained by the developed correlations with experimental and CFD results for several axial compressors whose data have been published in the open literature.

Validations Cases for the Deviation Model

Test Case 1: The Sulzer Four-Stage Compressor [14]. As mentioned earlier, the IGVs consist of 18 NACA65 blades with relative thickness $t/c = 1.2$. Each blade has a constant camber angle of 42.3 deg with solidity increasing from 1.54 at the hub to 0.73 at the tip. The inlet Mach number is ~ 0.45 . Comparison between the correlation and CFX results (Fig. 20) shows very good agreement in the midspan and the shroud regions. Larger differences between the CFD data and the prediction by the correlation occur in the hub region. Obviously, the influence of the viscous secondary flows in this region is much greater in the case of CFD calculations than was predicted by the correlations.

Test Case 2: The LUH Three-Stage Experimental Compressor. The IGVs consist of 26 highly twisted blades with NACA65-10 airfoils as described previously. The comparison between the correlation and the CFX predictions is shown in Fig. 21. The blades have a large nonlinear variation of camber angle from ~ 0 deg at the hub to >50 deg near the shroud. In contrast to test case 1, here the induced flow model plays a crucial role.

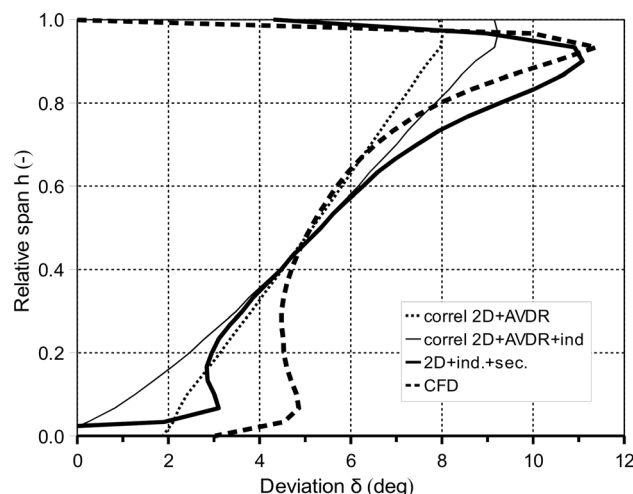


Fig. 20 Deviation prediction: the developed correlation and CFD results for Sulzer four-stage compressor IGVs (test case 1)

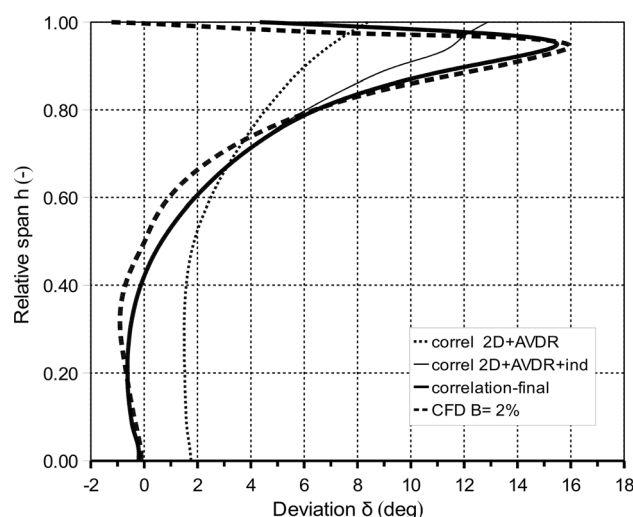


Fig. 21 Comparison between the developed correlation and CFD results—LUH three-stage compressor IGV deviations (test case 2)

Test Case 3: A Simple IGV Device From the Experimental Compressor Stage Described in [16]. The blades are formed from thin sheet plates bent to have a constant radius circular-arc camber. The camber was varied to give the required prerotation to the air at each radius by adjusting the chord length. The camber angle increases from 18 deg at the hub to 28 deg at the shroud. The inlet metal angle is large, in the range of 8 deg–10 deg. The axial velocity, density ratio is significantly higher than unity, and therefore, the AVDR correction has an important impact on the final results. The cascade solidity is ≈ 1.5 all over the span. The deviation was calculated as for NACA65 with a circular-arc camber line and with correction for relative thickness, which is about 0.003. A comparison of the IGV deviations predicted by the correlation developed here, CFD, and experimental data is presented in Fig. 22.

Test Case 4: IGV From a Supersonic Compressor for an XJ55-FF-1 Turbojet Engine With 27 NACA65 Blades [17]. The hub-to-shroud radius ratio is 0.77 and the solidity decreases in the range 1.47 – 1.13 from the hub to the shroud. The blade camber angle decreases linearly from 30 deg at the hub to 0 deg at the shroud. A comparison between the correlation, CFD and experimental data is presented in Fig. 23.

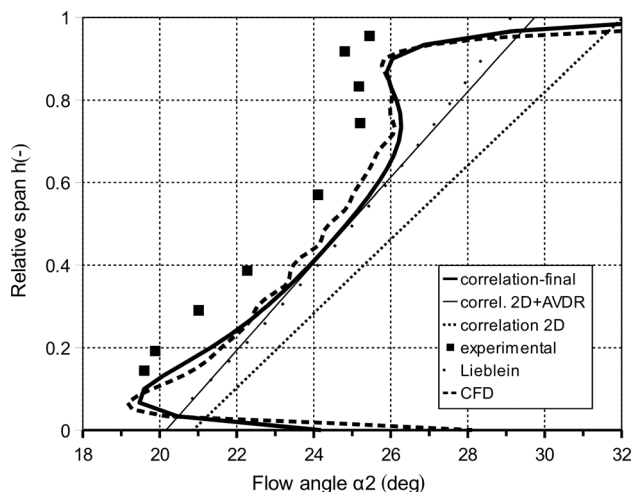


Fig. 22 Deviation prediction—the developed correlation and experimental data for IGVs consisting of thin sheet plates, test case 3

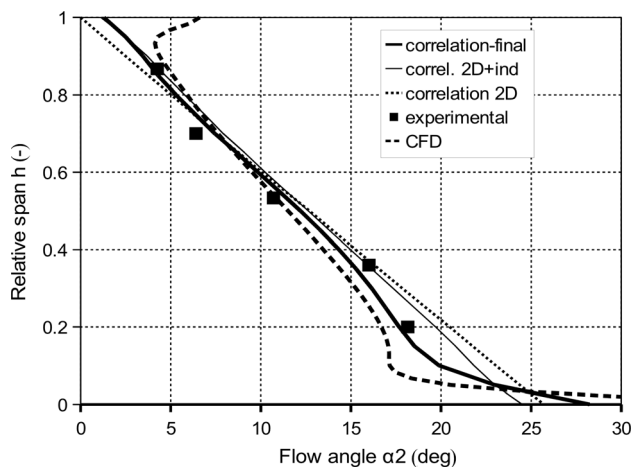


Fig. 23 Exit flow angle: comparison between the correlation and experimental data for test case 4

Test Case 5: IGVs Described in Ref. [18] Consisting of 22 NACA63 A4K6 Blades. The hub to shroud radius ratio is 0.74 and the solidity is 0.75 and is constant over the whole span. Other geometry parameters change almost linearly over the span: the stagger angle increases from 0.6 to 12deg and the blade lift coefficient increases from 0.88 to 1.125.

Figure 24 shows the results for the IGV exit angle obtained using the correlation, CFD calculation and the experimental data from Ref. [18]. The small disagreement between the experimental data and the correlation in the near-hub zone is caused by the presence of a nonshrouded blade tip clearance, which was not included in the correlations.

Validation Cases for the Loss Model. Two IGV rows already described are taken as test cases for validation of the loss model. The correlation developed here is compared only with CFD results, in the absence of experimental data. We found this to be sufficient since the loss correlation is of secondary importance compared with the deviation model.

Test Case 1. The Sulzer four-stage compressor has a conventional blade row, with almost constant outflow angle over the span. Figure 25 shows basic 2D losses, predicted by correlation (31). Two-dimensional losses are slightly higher near the hub,

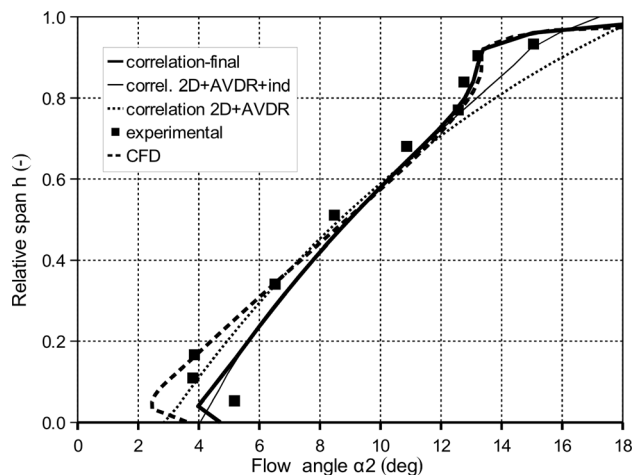


Fig. 24 IGV exit angle—comparison of the correlation and experimental data for test case 5

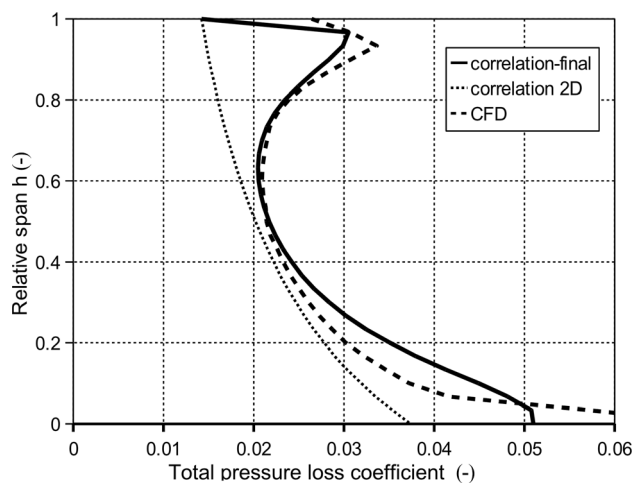


Fig. 25 Loss coefficient for Sulzer four-stage compressor IGV, test case 1

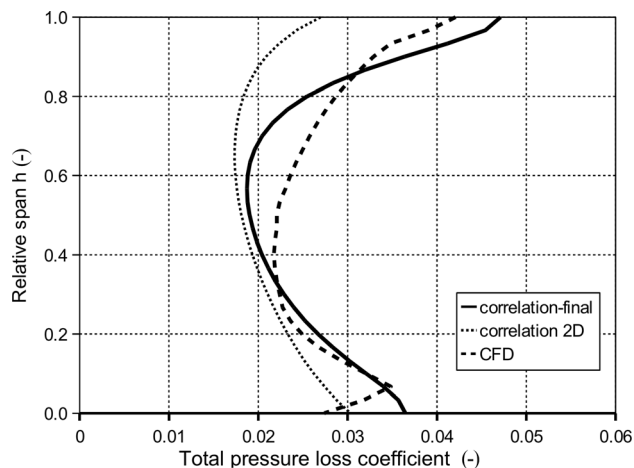


Fig. 26 Loss coefficient for LUH three-stage compressor IGV, test case 2

because of the higher solidity, while the low solidity in the near-shroud region gives larger secondary losses. However, the comparison between the correlation and CFX results shows good agreement throughout the span.

Test Case 2. The LUH three-stage experimental compressor has highly twisted blades. Comparison of the prediction by correlation (31) and CFX results is shown in Fig. 26. Two-dimensional losses are large in the near-hub region (low turning but high solidity) and in the near shroud region (high turning), while the secondary flow losses are not present in the near hub zone because of the absence of flow deflection.

For a good prediction of overall machine performances, it is sufficient to have a rough guess of IGV losses, whereas the deviation has to be calculated as accurately as possible. This conclusion is the consequence of the small absolute value of the total pressure losses in IGVs. Although the total pressure loss coefficient is relatively large, the absolute decrease in the total pressure is usually small due to low value of the inlet velocity and the inlet dynamic pressure.

Losses in IGV rows play an important role only in the case of operation at low-speed partial loads, with large stagger angle adjustments.

Conclusions

In this paper, a new and systematic methodology for prediction of inlet guide vane performance is described. Sets of correlations to calculate the IGV exit flow angle deviation and total pressure loss were created in such a way as to include a wide range of geometry and operating condition parameters and their influences. Three profile types are included in the model: NACA65; NACA65 with circular-arc camber line, which are often used for compressor blade rows; and NACA63 A4K6 airfoils that are designed for use in accelerating blade rows. Reference loss and deviation correlations, which include the main geometry parameters and Mach number influence, are supplemented by correlations for additional losses and deviation due to stagger angle adjustments for off-design operation.

For validation of the model, a number of test cases with configurations were considered. The comparison of the results obtained from the presented correlations with experimental and CFD results shows reasonably good agreement throughout. The results suggest that the method can be used successfully as part of design tools for axial compressors. It is expected that the application of the method could significantly improve the quality and reliability of the overall compressor through-flow results.

Nomenclature

- AVDR = axial velocity density ratio: $(c_{2a}\rho_2)/(c_{1a}\rho_1)$
 B = blockage factor
 c = velocity
 c = blade profile chord length
 C = correction coefficient in induced flow model
 C_{amp}, C_{av} = amplification and averaging coefficients
 C_{lo} = lift coefficient for single airfoil
 h = relative spanwise position $(r - r_H)/(r_T - r_H)$
 H = row (or cascade) absolute height $(r_T - r_H)$
 h^* = corrected relative spanwise position
 i = incidence angle
 K = induced flow model correction factor
 Ma_1 = inlet Mach number
 n = number of blades in a row
 N = number of discrete radial positions
 p = pressure
 s = blade spacing
 r = radial coordinate
 Re_c = Reynolds number based on a chord length
 t = blade profile maximum thickness
 w = flow complex potential
 y = absolute spanwise coordinate for a linear cascade
 z = complex coordinate in potential flow model
 α = flow angle
 γ = blade stagger angle

- γ = factor of blade circulation change rate
 δ = exit flow angle deviation $\kappa_2 - \alpha_2$
 δ^* = boundary layer displacement thickness
 θ = boundary layer momentum thickness
 κ = blade metal angle
 ρ = density
 σ = cascade solidity c/s
 ϕ = blade camber angle
 ϖ = total pressure loss coefficient: $(p_1^\circ - p_2^\circ)/(p_1^\circ - p_1)$
 Ω = stagger angle adjustment $\gamma - \gamma_o$

Directions

- a = axial component
r = radial component
u = circumferential, tangential component
x = pitchwise component normal to main flow

Subscripts

- H = hub position
l = lower
o = current, local radial position
t = thickness correction
T = tip (shroud) position
u = upper
0 = reference, optimal value
1 = row inlet
2 = row outlet

Superscript

- ind = induced

Appendix A

Induced Flow Analytical 2D Model. The analytical model for a linear cascade flow has to be studied to obtain the relation between the induced velocity on the trailing edge for a single blade model and then for the linear cascade. Similarly, the pitchwise distribution of induced velocity is needed for the relation between the value of the pitchwise velocity on a local trailing edge and its blade-to-blade averaged value.

The analytical model is based on a continually distributed system of constant strength vortices, spanned over each trailing edge. For a linear cascade having a blade spacing s and height H , the complex potential is

$$w(z) = -\frac{i\chi}{2\pi} \sum_{n=-\infty}^{+\infty} \left[\int_{ns}^{ns+iH} \ln(z_o - z) dz - \int_{ns+iH}^{ns+2H} \ln(z_o - z) dz - \int_{ns-iH}^{ns} \ln(z_o - z) dz \right]$$

where z_o represents an independent point and z is a point located on a reference trailing edge, $z \in [0, H]$. The pitchwise coordinate of an arbitrary trailing edge is ns , where n is the number of the trailing edge. The factor χ is a constant value of the circulation change rate $d\Gamma/dy$. On the hub and the shroud position for $y = 0$ and $y = H$, the flowfield potential mirror images are applied to include the influence of end walls as shown in Fig. 13.

Example flowfield streamlines for a cascade with the dimensions $H = 80$ mm, $s = 40$ mm, and consisting of an infinite number of blades are shown in Fig. 27(a). The axial velocity is constant, $c_a = 100$ m/s, and the circulation is calculated for spanwise velocity linear growth from 0 m/s on the hub to 36.4 m/s at the tip, corresponding to a flow angle $\alpha_2 = 20$ deg (i.e., the circulation

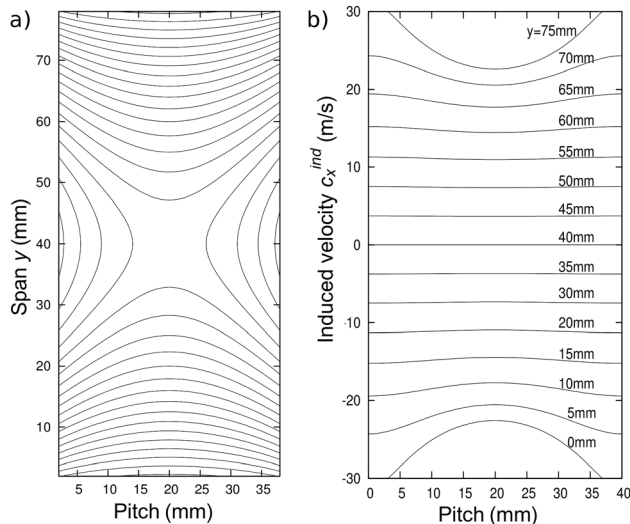


Fig. 27 Streamlines for induced secondary flow (a) and pitchwise distribution for the x component of induced velocity (b), $H/s = 2$

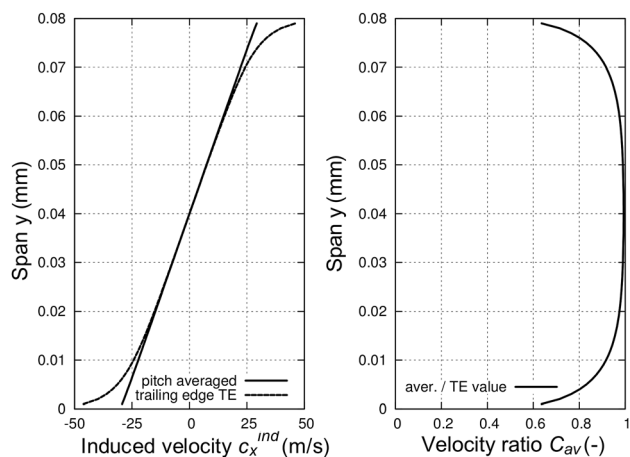


Fig. 28 Velocity c_x^{ind} ; comparison between the local, trailing edge value and pitchwise averaged value. Cascade with $H/s = 2$.

variation is linear from $\Gamma = 0$ at the hub to $\Gamma = 1.456 \text{ m}^2/\text{s}$ at the shroud). Figure 27(b) shows the x component of the velocity over the exit plane domain.

Figure 28 shows the difference between induced velocity on the trailing edge $c_x^{ind}|_{x=0}$ and $\overline{c_x^{ind}}$, which is the value averaged over the pitch $x \in [0, s]$.

Both values are for a system with an infinite number of blades. The averaging factor for a local spanwise position y_o is $C_{av} = \overline{c_x^{ind}}/c_x^{ind}|_{x=0}$.

The local trailing edge induced velocity is affected by other trailing edge vortex systems and amplified depending on the cascade solidity, i.e., the H/s ratio. The factor C_{amp} is introduced when the induced velocity on the trailing edge for a cascade with an infinite number of blades $c_x^{ind}|_{x=0}$ is divided by the analogous value for the single blade case. Both of these values are defined for a system with end wall mirror images and the resulting factor is $C_{amp} = c_x^{ind}|_{x=0}^{cascade}/c_x^{ind}|_{x=0}^{single}$. The H/s ratio is an important parameter for both factors C_{av} and C_{amp} . The final correction is given as the product of these two factors, as shown in Fig. 29.

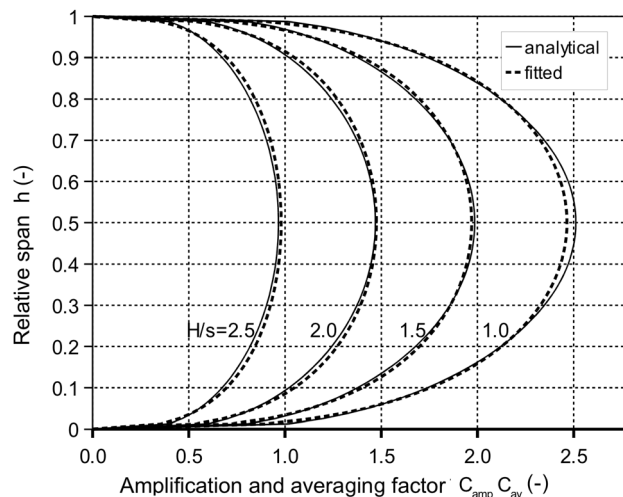


Fig. 29 Variation of averaging and amplification factors together over the blade span

The analytical results were fitted to find a simple equation to be used in the final model:

$$C_{amp}C_{av} = 1.566 \cdot (H/s)(h(1-h))^{0.3308} \quad (A1)$$

Development of the Correlation. Now we can return to the derivation of the equations for the final model for an annular cascade. The blade-to-blade velocity component c_x^{ind} is the main interest here. The spanwise change of a circulation for one blade can be expressed as

$$\frac{d\Gamma}{dr} = \frac{2\pi}{n} c_a \frac{d}{dr} (rtg\alpha_2) = \frac{2\pi}{n} c_a \gamma, \quad (c_a \approx \text{constant})$$

The simplest way to simulate a trailing edge vortex system would be to use a finite number of discrete vortices with finite circulations $\Delta\Gamma_i$. However, we have found this approach to be too sensitive to the numerical accuracy and quality of the geometry input data. Undesirable, step-shaped results were obtained in few cases. Therefore, a different approach was applied here and it is discussed further below.

If we integrate the circulation change over a small segment from r_l to r_u (Fig. 14) considering the circulation change parameter $\gamma = d(rtg\alpha_2)/dr$ to be constant, then we have

$$c_x^{ind} = \frac{1}{4\pi} \int_{r_l}^{r_u} \frac{1}{r_o - r} \frac{d\Gamma}{dr} dr = \frac{1}{2n} c_a \gamma \int_{r_l}^{r_u} \frac{1}{r_o - r} dr$$

The cumulative value for velocity at point O , induced from N continuous vortex segments, is

$$\frac{c_u^{ind}}{c_a} = \frac{1}{2n} \sum_{i=1}^N \gamma_i \ln \left| \frac{r_o - r_l}{r_o - r_u} \right| \quad (A2)$$

To obtain the final Eq. (19), the end wall mirror images of a flow-field have to be included in Eq. (A2). Then, this value has to be multiplied by an amplification and an averaging factor. Also, it has to be significantly corrected for real 3D flow and viscous effects.

Trailing edge vortex filaments are not perpendicular to the cascade exit plane. This influence is eliminated by the blades to the left and right of the local trailing edge. However, vortex filaments are not semi-infinite straight rays. They are carried by the

perturbed flow and, more importantly, their circulation is rapidly decreased downstream since they are eliminated by the viscous forces. The final correction coefficient is

$$C = K \cdot C_{\text{amp}} C_{\text{av}} = 0.1167 \cdot C_{\text{amp}} C_{\text{av}}$$

The correction factor $K = 0.1667$ is chosen on the basis of the final model calibration.

Appendix B

Preview of the Loss and Deviation Model

Reference incidence:

NACA65 and NACA65 with circular camber line	NACA63 A4K6
$i_0 = (0.025 \cdot \sigma - 0.06) \cdot \phi$	$\gamma_0 = \frac{17.702C_{i_0}}{1 + 0.4987\sigma^{-1.0724}}$
$\gamma_0 = \phi/2 + i_0$	$i_0 = \gamma_0 - \text{tg}(0.4749C_{i_0})$

Reference correlation:

$$\delta_0 = (a + b \cdot \sigma + c \cdot \text{Ma}_1) \cdot \phi^{(d+e \cdot \sigma + f \cdot \text{Ma}_1)}, \phi \geq 0$$

$$\varpi_0 = \exp(a + b \cdot \phi + c \cdot \sigma + d \cdot \text{Ma}_1) + e \cdot \sigma$$

Thickness correction:

$$\Delta\delta_t = (a + b\sigma)(d - (t/c)) \frac{\phi}{c} (f\text{Ma}_1 + g)$$

$$\Delta\varpi_t = (a - b\sigma)(d - t/c)(e\text{Ma}_1 - f)$$

Non reference incidence correlation: $\Omega = i - i_0$

$$\Delta\delta_\Omega = (a + b\phi^2 + c\sigma + d\sigma^2 + e\phi \cdot \Omega^f) \cdot \Omega$$

$$\Delta\varpi_\Omega = 0.0002 \cdot 1.48\Omega \cdot 0.09\sigma \cdot (1 + 0.01 \cdot \phi)$$

$$\Delta\varpi_{\text{stall}} \approx 0.12 + 0.007\phi$$

2D correlation:

$$\delta_{2D} = \delta_0 + \Delta\delta_t + \Delta\delta_\Omega$$

$$\varpi_{2D} = \varpi_0 + \Delta\varpi_t + \Delta\varpi_\Omega$$

AVDR correlation: $\Delta\delta_{\text{AVDR}} = 10 \cdot (\text{AVDR} - 1)$

Correlation for induced secondary flows:

$$(\Delta\delta_{\text{ind}})_o = \arctg\left(\cos \alpha_{2,o} \cdot \frac{c_{s,\text{ind}}}{c_a}\right)$$

$$\frac{c_{s,\text{ind}}}{c_a} \Big|_o = C \frac{1}{2n} \sum_{i=2}^{N-1} \gamma_i \ln \left| \frac{(r_o - r_l)(r_o - 2r_H + r_l)(r_o - 2r_T + r_l)}{(r_o - r_u)(r_o - 2r_H + r_u)(r_o - 2r_T + r_u)} \right|$$

$$\gamma_i = (r_{i+1} \text{tg} \alpha_{2,i+1} - r_{i-1} \text{tg} \alpha_{2,i-1}) / (r_{i+1} - r_{i-1})$$

$$C = K \cdot C_{\text{amp}} C_{\text{av}} = 0.261 \cdot (H/s)(h(1-h))^{0.3308}$$

Correlation for viscous secondary flows:

$$\Delta\delta_{\text{sec}} = 1.51C_{\kappa 2}(1 - e^{-0.032\Delta x})[\xi(h) + \xi(1-h)]$$

$$C_{\kappa 2} = 1 + 0.001(h - 0.5) \frac{d\kappa_2}{dr}, (\kappa_2[\text{deg}], r[m])$$

$$\xi(h) = (a + bB)\ln(c + d \cdot B + h^*) \cdot (e + fB)^{h^*}, B \geq 0.01$$

$$h^* = 0.6(H/s)h$$

$$\Delta\varpi_{\text{sec}} = 0.0064 \cdot 1.026^{\Delta x} (s/H) \cdot \eta(h)$$

$$\eta(h) = 6e^{-8h} - 4e^{-16h} + 6e^{-8(1-h)} - 4e^{-16(1-h)}$$

Final correlation:

$$\delta = \delta_0 + \Delta\delta_t + \Delta\delta_\Omega + \Delta\delta_{\text{AVDR}} + \Delta\delta_{\text{ind}} + \Delta\delta_{\text{sec}}$$

$$\varpi = \varpi_0 + \Delta\varpi_t + \Delta\varpi_\Omega + \Delta\varpi_{\text{sec}}$$

All the equations have different coefficients, which are given in the main part of the paper. All the angles are in degrees.

References

- [1] Lieblein, S., 1950, "Turning Angle Design Rules for Constant-Thickness Circular-Arc Guide Vanes in Axial Annular Flow," Lewis Flight Propulsion Laboratory, Cleveland, OH, Paper No. NACA TN 2179.
- [2] Zimmey, C. M., and Lappi, V. M., 1945, "Data for Design of Entrance Vanes From Two Dimensional Tests of Airfoils in Cascade," NACA Advance Confidential Report L5G18.
- [3] Waltke, U., 1995, "Berechnung des Meridianströmungsfeldes in Axialverdichtern mit der Methode der Finiten Elemente," Fortschritt-Berichte VDI Reihe 7 Nr. 261, VDI-Verlag, Düsseldorf, Germany.
- [4] Petrovic, M. V., Wiedermann, A., and Banjac, M., 2009, "Development and Validation of a New Universal Throughflow Method for Axial Compressors," ASME Paper No. GT2009-59938.
- [5] Lieblein, S., 1965, "Experimental Flow in Two-Dimensional Cascades," *Aerodynamic Design of Axial-Flow Compressors*, I. A. Johnsen and R. O. Bullock, eds., NASA Lewis Research Center, Cleveland, OH, NASA SP-36, pp. 183–225.
- [6] Drela, M., and Youngren, H., 1998, *A User's Guide to MISES*, MIT Computational Aerospace Sciences Laboratory, Cambridge, MA.
- [7] Bruna, D., Turner, M. G., and Cravero, C., 2006, "The Development of an Aerodynamic Performance Prediction Tool for Modern Axial Flow Compressor Profiles," ASME Paper No. GT2006-90187.
- [8] Pitzinger, W. E., 1998, "Kennfeldberechnung für Axialverdichter mit systematischer Untersuchung der Verlust und Umlenkeigenschaften von Schaufelgittern," Fortschritt-Berichte VDI Reihe 7 Nr. 337, VDI-Verlag, Düsseldorf, Germany.
- [9] Camp, T. R., and Shin, H.-W., 1995, "Turbulence Intensity and Length Scale Measurements in Multistage Compressors," ASME J. Turbomach., **117**, pp. 38–46.
- [10] Aungier, H. R., 2003, *Axial-Flow Compressors*, ASME Press, New York.
- [11] Dunavant, C. J., 1957, "Cascade Investigation of a Related Series of 6-Percent-Thick Guide-Vane Profiles," Langley Aeronautical Laboratory, Langley Field, VA, NACA TN 3959.
- [12] Mattiske, B., 1994, "Experimentelle Untersuchung einer mehrstufigen Axialverdichterbeschufelung mit Randzonen-Korrektur," Fortschritt-Berichte, VDI Reihe 7, Nr. 252, VDI-Verlag, Düsseldorf, Germany.
- [13] Lieblein, S., and Ackley, R. H., 1951, "Secondary Flows in Annular Cascades and Effects on Flow in Inlet Guide Vanes," Lewis Flight Laboratory, Cleveland, OH, NACA RM E51G27.
- [14] Hirsch, C., and Denton, J. D., 1981, "Through Flow Calculations in Axial Turbomachines," AGARD-AR-175, pp. 229–255.
- [15] D'Ippolito, G., Dossena, V., Mora, A., 2011, "The Influence of Blade Lean on Straight and Annular Turbine Cascade Flow Field," ASME J. Turbomach., **133**(1), p. 011013.
- [16] Mahoney, J. J., Dugan, P. D., Budinger, R. E., and Goelzer, F. H., 1950, "Investigation of Blade-Row Flow Distributions in Axial-Flow-Compressor Stage Consisting of Guide Vanes and Rotor-Blade Row," Lewis Flight Propulsion Laboratory, Cleveland, OH, NACA RM E50G12.
- [17] Graham, R. C., and Tysl, E. R., 1949, "Performance of Axial-Flow Supersonic Compressor of XJ55-FF-1 Turbojet Engine II—Performance of Inlet Guide Vanes as Separate Component," NACA, Washington, DC, NACA RM SE9E03.
- [18] Lawrence, J. J., and Theodore, E. F., 1957, "Experimental Investigation of Performance of Single-Stage Transonic Compressor With Guide Vanes Turning Counter to Direction of Rotor Whirl," Lewis Flight Propulsion Laboratory, Cleveland, OH, NACA RM E57B04.